Journal of Science: Advanced Materials and Devices 6 (2021) 202–208

Contents lists available at ScienceDirect

Journal of Science: Advanced Materials and Devices

journal homepage: www.elsevier.com/locate/jsamd

Original Article

Tailoring optical and resistance properties of the functional $CuAl_xO_y$ semiconductor for applications as thermal infrared imagers

Viet Hoang Vu [a, b, 1], Bao Quang Tu [b, 1], Quyen Xuan Phung [a, 1], Vinh The Tran [a], Nghia Nhan Hoang [a], Dat Dinh Pham [a], Tuan Anh Mai [c], Hien Duy Tong [d], Minh Van Nguyen [e], Hung Quoc Nguyen [a], Hue Minh Nguyen [f], Huy Van Mai [f], Dung Chi Duong [f], Quang Minh Doan [g], Thuat Nguyen-Tran [a, *]

[a] Nano and Energy Center, VNU University of Science, Vietnam National University, Hanoi, 334 Nguyen Trai Street, Thanh Xuan District, Hanoi, Viet Nam
[b] Department of Fundamental and Applied Sciences, University of Science and Technology of Hanoi, Vietnam Academy of Science and Technology, 18 Hoang Quoc Viet, Cau Giay, Hanoi, Viet Nam
[c] Microfabrication Laboratory and Pilot Plant Center, National Center for Technological Progress, 25 Le Thanh Tong Street, Hoan Kiem District, Hanoi, Viet Nam
[d] Materials Science Program, Vietnamese German University, Le Lai Street, Hoa Phu Ward, Binh Duong New City, Binh Duong Province, Viet Nam
[e] Department of Physics, Faculty of Basic and Fundamental Sciences, Viet Nam Maritime University, 484 Lach Tray, Hai Phong, Viet Nam
[f] Le Quy Don Technical University, 236 Hoang Quoc Viet, Cau Giay District, Hanoi, Viet Nam
[g] Faculty of Physics, VNU University of Science, Vietnam National University, Hanoi, 334 Nguyen Trai Street, Thanh Xuan District, Hanoi, Viet Nam

ARTICLE INFO

Article history:
Received 18 October 2020
Received in revised form
5 January 2021
Accepted 13 January 2021
Available online 19 January 2021

Keywords:
TCR
Oxide semiconductor
Micro-bolometers
Uncooled thermal imager
UFPA

ABSTRACT

This is the first report on the optical and resistance properties of copper aluminum oxide thin films for applications as thermal infrared imagers. The deposition of these films was investigated under three series of reactive magnetron sputtering conditions. Structural characterization identified the P63mmc hexagonal crystalline structure of $CuAlO_2$ although the 150- to 350-nm thick films were in a non-stoichiometric $CuAl_xO_y$ ratio. The thermal coefficient of resistance of the $CuAl_xO_y$ films was measured to be in the range 1.7–2.2%/K and the resistivity ranged from 0.3 to 1.0 Ω cm with n-type nature. To explain the low indirect bandgap value of the $CuAl_xO_y$ films, a type-I band alignment bulk heterojunction between $CuAlO_2$ and Cu_2O is proposed. This provides an effective method to decrease the resistivity and increase the thermal coefficient of resistance. From their optical characterization, a refractive index of 2.27 ± 0.07 was deduced, thus favoring the $CuAl_xO_y$ films for antireflection coating in the long infrared wavelength region. A micromachining process of $CuAl_xO_y$ micro-bridges was demonstrated with well-defined shapes at a pixel pitch of 25 μm. These findings pave the way for the future development of high-performance thermal infrared imagers.

1. Introduction

Uncooled thermal infrared imagers, or uncooled focal plane arrays (UFPAs), are devices allowing us to capture the temperature distribution of a scene without cooling. Since their inception, UFPAs were not believed to be competitive against cooled thermal infrared imagers because of their limited ability to simultaneously improve spatial resolution and temperature resolution [1]. Nevertheless, thanks to their room temperature operation, UFPAs have gained tremendous attention as well as a very large spectrum of applications [2]. The fabrication of UFPAs relies heavily on surface micromachining technology, which in turn has been leveraged by the development of the complementary metal oxide semiconductor (CMOS) industry [3–5]. The technological readiness of UFPAs is at a very high level [6] with the participation of very active main players in the market [7–12]. However, newcomers are willing to enter the market since the needs of UFPAs are quite specific regionally and nationally [13,14].

* Corresponding author. Nano and Energy Center, VNU University of Science, Vietnam National University, Room 503, 5th floor, T2 building, 334 Nguyen Trai street, Thanh Xuan, Hanoi, Viet Nam. Fax: +84 435 406 137.
E-mail address: thuatnt@vnu.edu.vn (T. Nguyen-Tran).
Peer review under responsibility of Vietnam National University, Hanoi.
[1] These authors contribute equally to the work.

https://doi.org/10.1016/j.jsamd.2021.01.004

The room temperature operation condition and the working mechanism of UFPAs require that they possess the following criteria: (i) high absorption of radiation in the long wavelength infrared region (LWIR), (ii) high thermal isolation of the sensing element, and (iii) high thermal coefficient of resistance (TCR) of the sensing element. Micro-devices composed of an UFPA, which have all of these three important criteria, are called micro-bolometers [6]. To attain high radiation absorption in the LWIR, micro-bolometers are often multilayered structures that act simultaneously in antireflection and absorption roles [15]. For high thermal isolation, micro-bolometers need to be suspended from the substrate carrying them [16]. A combination of absorption and suspension thus presents the idea of forming a quarter wavelength Fabry-Perot micro cavity in the thermal infrared region, whose central wavelength is around 10 μm [17]. Lastly, the resistive sensing mechanism of a micro-bolometer requires a thin film material with a high TCR value. Candidates responding to this criterion are semiconductor materials having high activation energies [18].

For micro-bolometers, amorphous silicon is the conventional choice since it is compatible with CMOS technology and its resistivity can be tuned by doping, thus allowing a wide range of selection for fabrication process. Amorphous silicon is often deposited in thin film form [9]. Another famous candidate for the sensing layer of a micro-bolometer is vanadium oxide (VO_x). The special property of VO_x is that vanadium possesses multiple oxidation states that inherently allow VO_x to shift its crystalline phase with changing temperature. As a result, the resistivity of VO_x changes accordingly with temperature, which leads to its high TCR value [19]. Together, amorphous silicon and VO_x are the main players in UFPA applications nowadays, however, there are still many choices for materials for the active layer of a micro-bolometer. For example, some choices are (i) ternary oxide semiconductor compounds like perovskites with a formula of ABO_3 [20] or spinels with a formula of AB_2O_4 [21], (ii) quaternary oxide compounds such as YBaCuO [22], (iii) composite graphene and carbon nanotubes based materials [23,24], and (iv) germanium-based materials [25].

There is another type of ternary compound semiconductor with a delafossite crystalline structure and formula of ABO_2 where A is a monovalent and B is a trivalent metal cation that has been well known in the literature for being a wide band gap p-type semiconductor compound for applications in transparent conductive oxides [26–30]. There have been many reports on the electrical properties of ABO_2 but a few of those have focused on its applications in micro-bolometers even though its temperature behavior of resistance was very interesting [31–34]. In this paper, we focus our efforts on a special type of a delafossite oxide semiconductor with a formula $CuAlO_2$ for the development of thermal infrared imagers. In comparison to our previous study [35] reporting on $CuFeO_2$, we have replaced the trivalent metal cation Fe^{3+} with Al^{3+}. The reason behind this replacement is the behaviour of ferromagnetic Fe, which can cause unwanted effects when applying these films in optoelectronic applications. In addition, there is a special property of $CuAlO_2$ in that the multi oxidation state of copper may allow $CuAlO_2$ to tune its resistivity with temperature, thus promising a high TCR value. Herein, we present the first thorough investigation of the optical and resistance properties of $CuAlO_2$ for applications as UFPAs. We demonstrate that the temperature behavior and refractive index at the LWIR of $CuAlO_2$, in combination with its capacity for surface micromachining fabrication, make it an excellent candidate as the active layer of a micro-bolometer.

2. Experimental

All $CuAl_xO_y$ thin film samples were deposited by reactive magnetron sputtering. The sputtering system, from Syskey, has four 2-in magnetron guns with two direct current (DC) sources for metal deposition and two radio frequency (RF) sources for oxide target deposition. The detailed sputtering conditions are presented in Table S1. Three series of samples were investigated, including one with varying sputtering power of the Cu_2O target (denoted as CuO-X), one with varying substrate temperature (denoted as TX00), and one with varying the sputtering power of both the Cu_2O and Al_2O_3 targets (denoted as AlCu-X).

The structural characterization of the thin film samples was carried out on an X-ray diffractometer (EQUINOX 5000, Thermo Scientific) with Cu-K_α X-ray radiation at 1.54056 Å of wavelength. The surface quality was investigated on a scanning electron microscopy system (SEM) (S4800, Hitachi) with elemental analysis by energy-dispersive X-ray spectroscopy (EDX). The temperature-dependent electrical measurements were performed on a four-point probe system (RM300, Jandel) with additional characterization by a Keithley 2400 source measurement unit and a customized temperature controller from 10 °C to 50 °C. The Hall measurement was carried out on a Hall system with Van der Pauw configuration (7700 series, Lakeshore). The thicknesses of all samples were characterized on a stylus surface profilometer (NanoMap 500LS, AEP Technology). Optical characterization was carried out on an ultraviolet-visible (UV-VIS) spectrometer (UV-26000, Shimadzu) and spectroscopic ellipsometer (SE) (SmartSE, Horiba Jobin Yvon). The SE adjustment was performed with DeltaPsi software (Horiba Jobin Yvon) using a conventional model composed by a substrate, a bulk layer containing all information about the thin film, and a roughness layer (50% of the bulk material and 50% of void). The demonstration of surface micromachining was performed with a process flow consisting of eight optical lithography and etching steps prior to the final release of micro-bridges for forming the desired micro-bolometers.

3. Results and discussion

Fig. 1a shows X-ray diffraction (XRD) patterns of the samples in the temperature series (XRD patterns of the other two series are illustrated in Fig. S1). There are no significant XRD peaks observed on the patterns except for one at about 35.5° and 38°. Nevertheless, a Rietveld analysis was performed (the details are shown in Fig. S2) for sample T200 (the same as the sample CuO-3) and allowed a decent structural extraction from the experimental XRD pattern. By using $CuAlO_2$ with a hexagonal crystalline structure with the space group P63mmc, known as the delafossite structure, the Rietveld refinement gave the lattice parameters of $a = b = 3.0029$ Å and $c = 11.4212$ Å (angles $\alpha = \beta = 90°$ and $\gamma = 120°$ are fixed by the space group P63mmc). As a result, we identified that the XRD peak at 35.5° corresponded to (101) reflection plane and the one at 38° corresponded to the (102) reflection plane of hexagonal P63mmc, which is quite similar to that reported in the literature [36]. The XRD patterns of other samples (except sample T700) of this temperature series exhibit the same feature, indicating that they share the same delafossite $CuAlO_2$ crystalline structure. The unit cell of this structure is presented in Fig. 1b (the detailed positions of each atom are provided in Table S2). We can easily recognize the usual layered structure of the delafossite ABO_2 (A is a monovalent and B is a trivalent metal cation) structure illustrated by the sandwiching of edge sharing Al_2O_3 octahedral layers and Cu_2O layers. In order to check if another crystalline phase of a copper aluminum oxide, copper oxide, or aluminum oxide compound individually exists in the thin films, a comparison with XRD powder patterns of those oxides is presented in Fig. S3. The result shows that the two intense peaks, 35.5° for (101) and 38° for (102), are by far best described by the delafossite $CuAlO_2$ hexagonal structure.

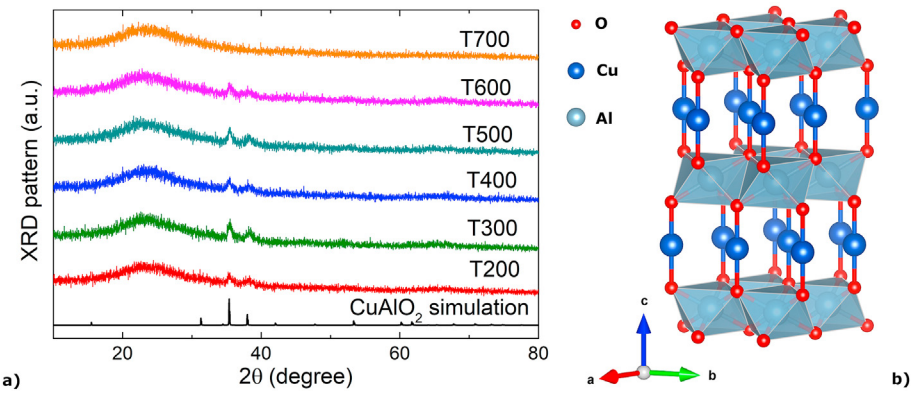

Fig. 1. (a) XRD patterns of the temperature series in comparison with the powder XRD simulation of $CuAlO_2$ based on the lattice parameters obtained from the Rietveld XRD refinement of sample T200 (details shown in Fig. S2). (b) The unit cell of the $CuAlO_2$ P63mmc hexagonal structure (details shown in Table S2) where the red atoms are oxygen, blue atoms are copper, and brown atoms are aluminum. Edge-sharing Al_2O_3 octahedral layers are sandwiched by Cu_2O layers.

Fig. 2 shows the temperature behavior of the resistance of all thin films in this study. For the temperature dependence from about 10 °C–50 °C, which is enough for uncooled infrared sensing applications, we observe a good linearity of the logarithm of the sheet resistance of the films as a function of temperature. This linearity is the basis for deducing the TCR values of the films, which are in the range from 1.7%/°C to 2.2%/°C (for simplicity here we refer to the absolute values of TCR instead of its real negative value). The semiconductor nature of the $CuAl_xO_y$ films is confirmed by the fact that the sheet resistance decreases when increasing the temperature. We can see that for the series changing the sputtering power of the Cu_2O target, when combined with the elemental characterization by EDX shown in Table S3, the highest TCR value corresponds to the lowest concentration of copper. It is normal that this concentration increases when increasing the Cu_2O target power but it is accompanied by a decrease of TCR value. For the substrate temperature series, the TCR value does decrease with increasing temperature. And for the third series, when the sputtering power of both oxide targets increases, the copper concentration increases and the TCR value becomes more important. Fig. 2d and e, respectively, show the dependency of TCR values with the sheet resistance and the resistivity of the $CuAl_xO_y$ films. The sheet resistance is important when practically optimizing these $CuAl_xO_y$ films for micro-bolometer applications, whereas the

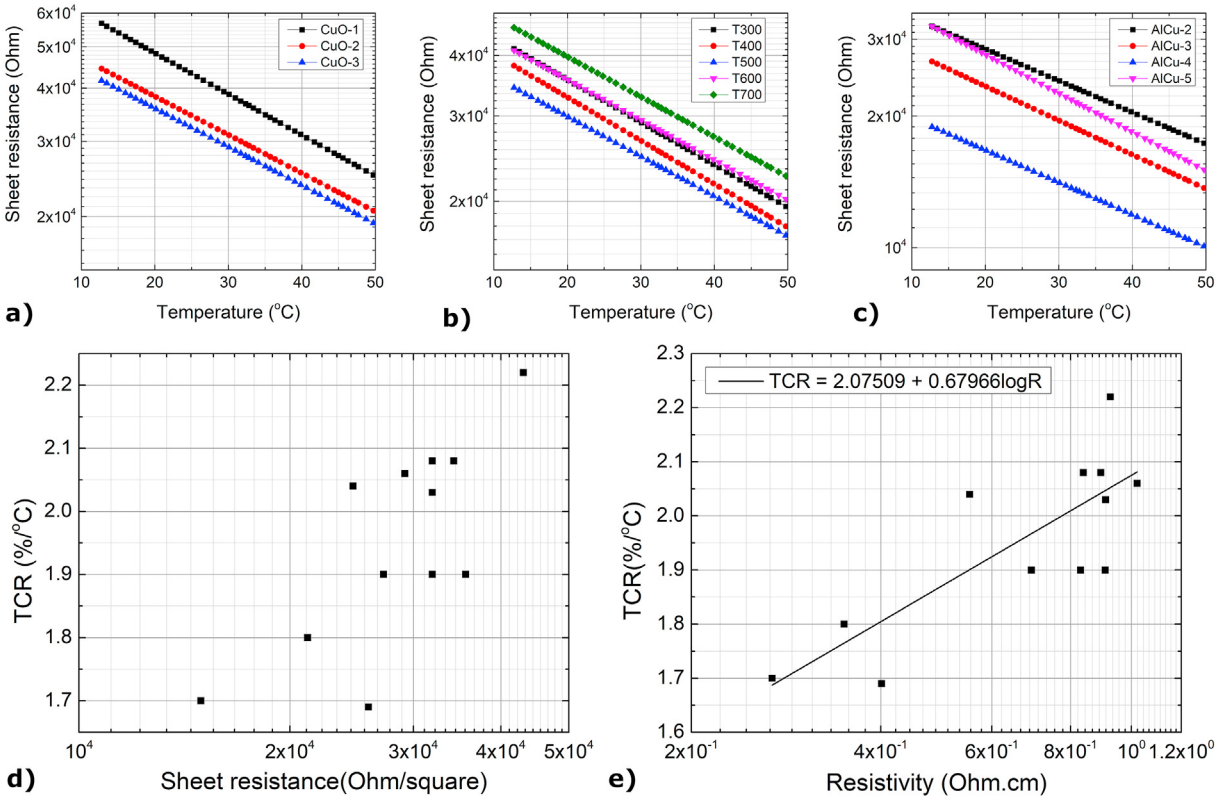

Fig. 2. Temperature dependence of the sheet resistance of thin films from three series: (a) sputtering power of the Cu_2O target, (b) sputtering temperature, (c) sputtering power of the Al_2O_3 and Cu_2O targets. Perfect linearity between the logarithm of the sheet resistance of the $CuAl_xO_y$ thin films and the temperature is observed thus showing its advantage for micro-bolometer applications. (d) TCR values versus the sheet resistance at 30 °C and (e) TCR versus the resistivity at 30 °C for all samples in three series.

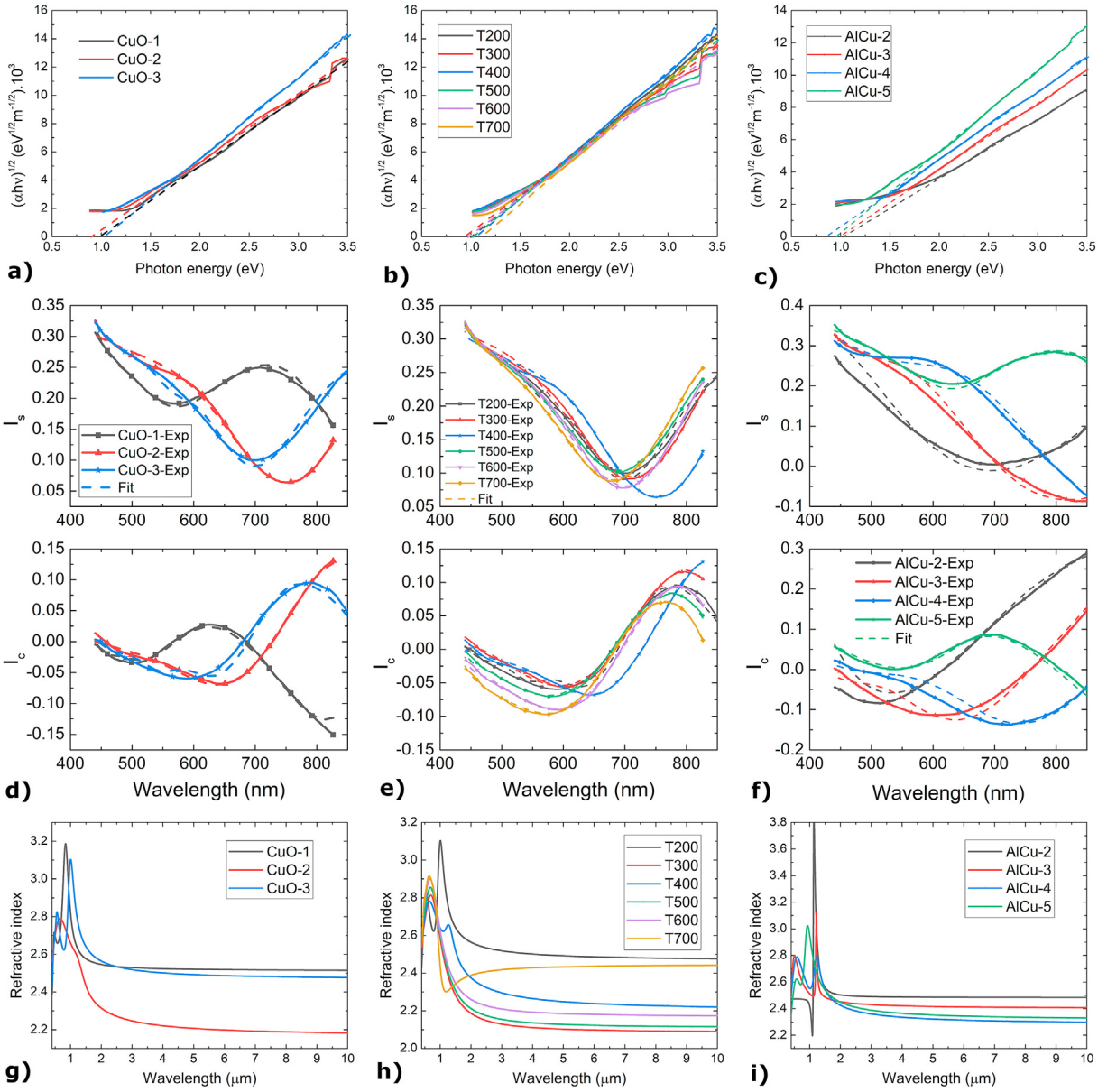

Fig. 3. (a)–(c) are the indirect band gap extrapolations of the $CuAl_xO_y$ thin films of the three series. (d)–(f) are the comparison of I_s and I_c normalized experimental intensities (solid lines) and the corresponding SE adjustment intensities based on a double amorphous dispersion function (dashed lines) of the three series, and (g)–(i) are the extrapolation of the refractive indices to the long infrared wavelength region by using the extracted parameters of the double amorphous dispersion function for the three series.

resistivity is better for fundamental studies on the nature of the resistance property. Depending on the circuitry of the uncooled thermal infrared sensors, the resistance of a microbolometer is generally in the range of 25 kΩ–95 kΩ, thus giving a range of sheet resistance from 12.5 kΩ/square to 47.5 kΩ/square (suppose that the micro-bolometer is composed mainly of a rectangular $CuAl_xO_y$ thin film with the width being half of the length). Fig. 2d shows that all $CuAl_xO_y$ films of the three series well satisfy this resistance condition. On the other hand, we can observe that the $CuAl_xO_y$ films deposited by sputtering in this study follow a general dependency between TCR values and resistivity, with higher resistivity producing higher TCR. In comparison to the resistivity of VO_x, which is in the range from 0.01 to 1 Ωcm [37], and to the resistivity of amorphous silicon, which is in the range from 100 to 10 k Ωcm [9], the $CuAl_xO_y$ films in this study lie in between 0.3 and 1.0 Ωcm. Furthermore, the Hall measurement with Van der Pauw pad configuration for one selected sample per experimental series revealed a *n-type* semiconductor nature of $CuAl_xO_y$. A carrier concentration value of 2.42 × 10^{18} cm^{-3} and a Hall mobility of 6.48 $cm^{-2}V^{-1}s^{-1}$ were found for CuO-3/T200 (TCR = 2.08%/°C) and a carrier concentration of 8.58 × 10^{18} cm^{-3} and Hall mobility of 4.08 $cm^{-2}V^{-1}s^{-1}$ for AlCu-4 (TCR = 1.70%/°C). By fitting the temperature dependence of sheet resistance for all samples, the activation energy E_a was deduced, which ranged from 132 meV to 175 meV (a typical fit is shown in Fig. S5).

Based on the thickness measurements performed on the profilometer (shown in Table S3) there is another correlation that we can deduce from the XRD patterns: the thinner the sample, the more difficult to obtain the pronounced XRD peaks. As a matter of fact, no XRD peak is found (Fig. S1) for the samples from the series with varying sputtering power of both oxide targets because they are quite thin. Another question that can be raised is a correlation

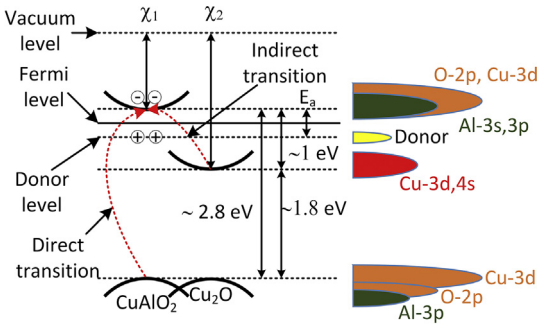

Fig. 4. A proposed schematic of electronic levels and PDOS of $CuAl_xO_y$ by considering phases of $CuAlO_2$ and Cu_2O in an amorphous matrix. In the intrinsic p-type nature, the electronic affinity of $CuAlO_2$ χ_1 is 2.5 eV and that of Cu_2O χ_2 is 3.2 [39,40]. When doped with donors, these affinities would increase by the same amount. Red color shows PDOS of Cu_2O only, green color shows $CuAlO_2$ only, orange color shows both Cu_2O and $CuAlO_2$, and yellow color shows the donor.

between the elemental characterization and XRD patterns. If hexagonal P63mmc is used to describe the structural properties of the $CuAlO_2$ sample T200, then the concentration of copper and aluminum must be equal. But this is not the case as shown in Table S3. Since no XRD peak for various copper oxides can be matched with the obtained XRD pattern (shown on Fig. S2), we suggest that the excess of copper oxide would be in an amorphous form. As a consequence, no crystalline peak was observed for all samples exhibiting an excess of copper oxide.

Fig. 3 shows optical characterizations of all $CuAl_xO_y$ films. Firstly, in order to estimate the bandgap of these films, the functions $(\alpha h\nu)^{1/2}$ are traced against photon energy. The absorption coefficient α was calculated based on the thicknesses, shown in Table S3, and the absorption spectra. The power 1/2 of $(\alpha h\nu)$ was chosen for characterizing an indirect bandgap material since we have revealed the amorphous nature of these films combined with a portion of the hexagonal phase of delafossite $CuAlO_2$ [38]. Secondly, the Tauc bandgap extrapolation was performed as the crossing point of the linear fit of $(\alpha h\nu)^{1/2}$ function with the horizontal axis (Fig. 3 from a to c). The values of indirect bandgap of $CuAl_xO_y$ are shown in Table S4. Fig. 3d–f exhibit the comparison of I_s and I_c normalized intensities between the experimental spectra and the one obtained by SE adjustment. The dispersion function used to describe $CuAl_xO_y$ is the double amorphous function (the detailed formula are presented in the electronic supplementary information). Values of the double amorphous function parameters (ε_∞, E_g, *A1*, *B1*, *C1*, *A2*, *B2*, *C2*) are presented in Table S4 as well as the adjustment quality X (the smaller the value of X, the better the adjustment). The parameter ε_∞ gives an estimation of the real part of the dielectric constant at an infinite photon wavelength. The parameter E_g is the estimation of the bandgap based on the double amorphous function. There is a good agreement between the experimental intensities (I_s and I_c) with the SE adjustment combined with a relatively low value of X (in Table S4). The difference in values of bandgap deduced from the extrapolation (Fig. 3a–c) and by the SE adjustment is relatively low. It is worth noting that the thicknesses of all samples are taken from the profilometer measurement and used as the fixed input thickness for the SE adjustment. Therefore, the SE adjustment performed here is reliable. Since the application of micro-bolometer is in the long wavelength region (up to 10 μm), an extrapolation of the refractive indices of all the films was performed as shown in Fig. 3g–i. A good tendency of refractive index when increasing wavelength is obtained for all samples investigated (except for T700). In order to estimate the refractive index of the $CuAl_xO_y$ films in the long wavelength region, we have taken the square root of the average real value of the dielectric constant at the infinite wavelength ε_∞ for all the samples. This value is equal to 2.27 ± 0.07, corresponding to ε_∞ = 5.15 ± 0.67. The extinction coefficient, on the other hand, is equal to zero for all photon energies smaller than the bandgap value. Thus, we used the zero value in the long wavelength region. The value of the refractive index of $CuAl_xO_y$ deduced here will play a central role in designing the antireflection coating layer on top of the $CuAl_xO_y$ layer when it is used in a real micro-bolometer.

In order to elucidate the low ~1 eV indirect band gap of this $CuAl_xO_y$ material, a direct band gap extrapolation was performed with the curves $(\alpha h\nu)^2$ versus photon energy. Bandgap values of ~2.8 eV were obtained, which are comparable with those reported previously for $CuAlO_2$ [26]. By combining the n-type nature, direct transitions around 2.8 eV, indirect transitions around 1 eV, and the electronic affinities of $CuAlO_2$ (2.5 eV) and Cu_2O (3.2 eV) found in the literature [39,40], a schematic of electronic levels of $CuAl_xO_y$ is illustrated in Fig. 4. The highest levels are the conduction band (CB) of $CuAlO_2$. From the obtained values of activation energy, we can identify a donor band, mainly due to the intentionally sputtered excess of metals in the material, lining from 132 meV to 175 meV below the CB of $CuAlO_2$. The Fermi level needs to be between donor levels and CB, thus all bands below the Fermi level are populated including the Cu-4s and the lower Cu-3d levels of CB of Cu_2O and the valence band of Cu_2O and $CuAlO_2$ (based on the reports about the partial density of states (PDOS) of Cu_2O and $CuAlO_2$ [41–44]). We suggest that the ~0.9–1 eV transition is (i) an intraband and indirect transition in the conduction band of Cu_2O or (ii) a cross transition from the bottom CB of Cu_2O to the CB of $CuAlO_2$. As a result, we propose that this $CuAl_xO_y$ material can be considered as a bulk heterojunction, with type I band alignment, between $CuAlO_2$ and Cu_2O in an amorphous matrix. Interestingly, if one could tune the donor levels, for example, to be closer to the bottom of the CB of Cu_2O, one could both increase the conductivity (by more electrons in the CB of Cu_2O embedded in the matrix) and the TCR (by enlarging the activation energy with respect to the CB of $CuAlO_2$). Finally, we would like to note that all samples became more transparent and much less conductive after annealing under ambient oxygen, thus highlighting the choice of Cu_2O over other types of copper oxides with higher values of oxidation.

Table 1 shows a comparative illustration of several main materials used in functional UFPAs with the $CuAl_xO_y$ material in this paper. $CuAl_xO_y$ thin films have a smaller refractive index in comparison to the refractive index of vanadium oxides in the range from 2.5 to 3 [45,46] and that of amorphous silicon (or polymorphous germanium silicon) in the range from 3.4 to 3.5 [47], thus they have certain advantage for antireflection in the long

Table 1
Comparative illustration of several main materials in UFPAs.

Material	TCR (%/°C)	Resistivity (Ω.cm)	Refractive index in the LWIR region
VOx	1–3 [37]	0.01–1.0 [37]	2.5–3 [45,46]
a-Si	2–5 [9]	100–10 k [9]	3.4–3.5 [47]
pm-Si_xGe_{1-x}	4.08 [48]	67 k [48]	N/A (from silicon to germanium) 3.4–4
$CuAl_xO_y$ (this work)	1.7–2.2	0.3–1.0	2.27 ± 0.07

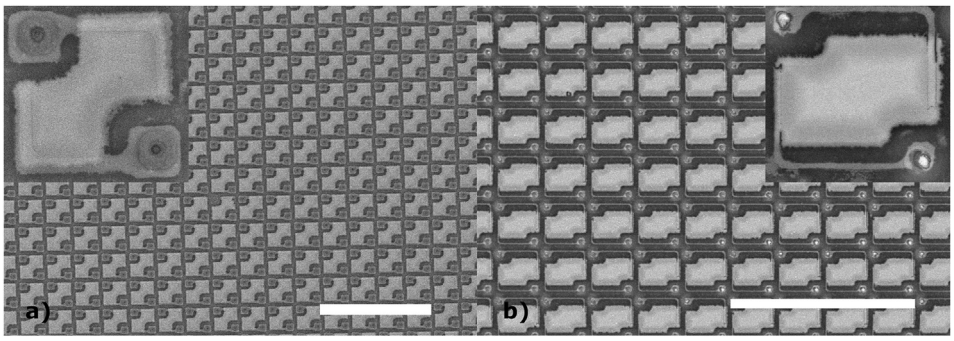

Fig. 5. SEM micrographs of micro-bolometers with 25 μm pitch obtained by eight photolithography steps with an active layer of $CuAl_xO_y$ and with two different active layer geometries. Inserted images are the corresponding pixels with dimensions of 25 μm × 25 μm. The scale bars are 100 μm.

wavelength region. In combination with the resistance properties, the $CuAl_xO_y$ films exhibit a slight edge in optical performance versus vanadium oxides and better resistance and optical properties versus amorphous silicon. Furthermore, with an interesting finding discussed earlier in this paper, $CuAl_xO_y$ could be considered as a bulk heterojunction with type I band alignment between $CuAlO_2$ and Cu_2O with the ability to increase both the conductivity and TCR at the same time. As a consequence, these $CuAl_xO_y$ films are a strong candidate for use in thermal infrared imagers.

Fig. 5 shows SEM micrographs of arrays of 25-μm micro-bolometers with two different geometries with the $CuAl_xO_y$ film as the active temperature sensing layer. This active layer is sandwiched between a supporting layer and an antireflection encapsulation layer. The supporting layer also includes a layer serving to absorb radiation in the long wavelength region. These arrays were obtained by at least eight photolithography steps for assuring the pattern of (i) row electrical channels, (ii) column electrical channels, (iii) various pathways from the active layer to electrical channels, and (iv) suspending structures for thermal isolation of the active layer in an improved process flow in comparison to our previous study [49]. It can be observed that the good micro-bolometer shapes were obtained, thus assuring that the $CuAl_xO_y$ films are well suited for micro-machining process flow for the fabrication of an array of micro-bolometers. The active layer, $CuAl_xO_y$, was effectively patterned in the last photolithography step, which assures the maximum stability of the TCR values of $CuAl_xO_y$. Further studies need to be completed in order to yield (i) a higher TCR value around from 4 to 5%/K, (ii) ohmic contacts between $CuAl_xO_y$ thin films and metal connections, (iii) better etching of $CuAl_xO_y$ thin films, and finally (iv) better releasing of $CuAl_xO_y$ micro-bridges.

4. Conclusion

Our experimental study on the $CuAl_xO_y$ semiconductor has revealed its enormous potential for applications as micro-bolometers and thermal infrared imagers. We found that the reactive sputtering conditions, including substrate temperature and sputtering power, had the remarkable influence on the resistance and optical properties of the $CuAl_xO_y$ films. The value of TCR was found to be around 2%/°C combined with a range of sheet resistance from 12.5 kΩ/square to about 47.5 kΩ/square. The $CuAl_xO_y$ material was of n-type with an activation energy ranging from 132 to 175 meV. The average value of the indirect bandgap was determined to be around 1 eV, which was also confirmed by spectroscopic ellipsometry adjustments. A type-I band alignment bulk heterojunction between $CuAlO_2$ and Cu_2O was proposed for explaining this low indirect band gap value. Based on the double amorphous dispersion function, we obtained an average refractive index value of 2.27 ± 0.07 in the long wavelength region. Regarding the compatibility of $CuAl_xO_y$ with photolithography-based surface micromachining, two different micro-bolometer geometries were fabricated with $CuAl_xO_y$ acting as the active layer. The good micro-bolometer shapes were achieved, enabling the future development of high-performance thermal infrared imaging sensors based on this class of $CuAl_xO_y$ materials.

Declaration of competing interest

The authors declare that they have no known competing financial interests or personal relationships that could have appeared to influence the work reported in this paper.

Acknowledgements

This research was supported by the Vingroup Innovation Foundation (VINIF) under the project code DA106_14062019/year 2019. The authors wish to express their sincere gratitude to Prof. M.H. Phan from the University of South Florida for his valuable guidance and constructive discussions throughout the project.

Appendix A. Supplementary data

Supplementary data to this article can be found online at https://doi.org/10.1016/j.jsamd.2021.01.004.

References.

[1] M. Kohin, N.R. Butler, Performance limits of uncooled VOx microbolometer focal plane arrays, in: B.F. Andresen, G.F. Fulop (Eds.), Infrared Technol. Appl. XXX, 2004, p. 447, https://doi.org/10.1117/12.542482.
[2] M. Kimata, Uncooled infrared focal plane arrays, IEEJ Trans. Electr. Electron. Eng. 13 (2018) 4–12, https://doi.org/10.1002/tee.22563.
[3] A.C. Fischer, F. Forsberg, M. Lapisa, S.J. Bleiker, G. Stemme, N. Roxhed, F. Niklaus, Integrating MEMS and ICs, Microsystems Nanoeng. 1 (2015) 15005, https://doi.org/10.1038/micronano.2015.5.
[4] F. Niklaus, C. Vieider, H. Jakobsen, MEMS-based uncooled infrared bolometer arrays: a review, Proc. SPIE 6836 (2007) 68360D, https://doi.org/10.1117/12.755128.
[5] L. Yu, Y. Guo, H. Zhu, M. Luo, P. Han, X. Ji, Low-Cost microbolometer type infrared detectors, Micromachines 11 (2020) 800, https://doi.org/10.3390/mi11090800.
[6] A. Rogalski, History of infrared detectors, Opto-Electron. Rev. 20 (2012) 279–308, https://doi.org/10.2478/s11772-012-0037-7.
[7] P.E. Howard, C.J. Han, J.E. Clarke, J.C. Stevens, P.A. Ely, E.T. Fitzgibbons, Advances in microbolometer focal plane technology at boeing, infrared detect. Focal pl, Arrays V 3379 (1998) 47, https://doi.org/10.1117/12.317613.
[8] C.A. Marshall, N.R. Butler, R.J. Blackwell, R. Murphy, T.B. Breen, Uncooled infrared sensors with digital focal plane array, Proc. SPIE 2746 (1996) 23–31, https://doi.org/10.1117/12.243059, 2746.

[9] J.-L. Tissot, F. Rothan, C. Vedel, M. Vilain, J.-J. Yon, LETI/LIR's uncooled microbolometer development, Infrared Technol. Appl. 3436 (XXIV) (1998) 605, https://doi.org/10.1117/12.328060.
[10] J.L. Tissot, A. Durand, T. Garret, C. Minassian, P. Robert, S. Tinnes, M. Vilain, High performance uncooled amorphous silicon VGA IRFPA with 17-μm pixel-pitch, in: B.F. Andresen, G.F. Fulop, P.R. Norton (Eds.), Proc. SPIE, 2010, p. 76600T, https://doi.org/10.1117/12.853063.
[11] C. Li, C.J. Han, G.D. Skidmore, C. Hess, DRS uncooled VOx infrared detector development and production status, in: B.F. Andresen, G.F. Fulop, P.R. Norton (Eds.), Proc. SPIE, 2010, p. 76600V, https://doi.org/10.1117/12.851795.
[12] U. Mizrahi, L. Bikov, A. Giladi, N. Shiloah, S. Elkind, T. Czyzewski, I. Kogan, S. Maayani, A. Amsterdam, I. Vaserman, Y. Hirsh, A. Fraenkel, New developments in SCD's 17-μm VOx μ-bolometer product line, in: B.F. Andresen, G.F. Fulop, P.R. Norton (Eds.), Proc. SPIE, 2010, p. 76600W, https://doi.org/10.1117/12.850705.
[13] L. Jiang, H. Liu, J. Chi, L. Qian, F. Pan, X. Liu, Design, fabrication and testing of 17 um pitch 640x480 uncooled infrared focal plane array detector, in: H. Gong, N. Wu, Y. Ni, W. Chen, J. Lu (Eds.), Proc. SPIE, 2015, p. 96740W, https://doi.org/10.1117/12.2199072.
[14] O. Celik, E. Inceturkmen, B. Kaplan, B. Barutcu, O. Aydin, I.E. Gonenli, R. Kepenek, C. Tunca, M. Akbulut, Ö.L. Nuzumlali, S. Keskin, K. Aydemir, C. Yildizak, 640 x 480 17 um microbolometer uncooled detector development at ASELSAN, Inc, in: G.F. Fulop, L. Zheng, B.F. Andresen, J.L. Miller (Eds.), Infrared Technol. Appl. XLVI, SPIE, 2020, p. 26, https://doi.org/10.1117/12.2557669.
[15] M. Aggoun, J. Jiang, M.K. Khan, Infrared absorption modeling of VOx microbolometer, Proc. SPIE (2015) 9620, https://doi.org/10.1117/12.2192816, 96200O.
[16] R.A. Wood, Uncooled thermal imaging with monolithic silicon focal planes, in: B.F. Andresen, F.D. Shepherd (Eds.), SPIE Vol. 2020, Infrared Technol. XIX, 1993, p. 322, https://doi.org/10.1117/12.160553.
[17] E. Mottin, A. Bain, J.-L. Martin, J.-L. Ouvrier-Buffet, S. Bisotto, J.-J. Yon, J.-L. Tissot, Uncooled amorphous silicon technology enhancement for 25-μm pixel pitch achievement, Infrared Technol. Appl. XXVIII (2003) 4820, https://doi.org/10.1117/12.464848, 200.
[18] W. Rehm, R. Fischer, J. Stuke, H. Wagner, Photo and dark conductivity of doped amorphous silicon, Phys. Status Solidi 79 (1977) 539–547, https://doi.org/10.1002/pssb.2220790218.
[19] C.W. Park, S. Moon, Analysis of multi-layer VOx thin film for uncooled IR detectors, J. Kor. Phys. Soc. 39 (2001) 138–140. http://pubs.kist.re.kr/handle/201004/16721.
[20] S. Liu, B. Guillet, A. Aryan, C. Adamo, C. Fur, J.M. Routoure, F. Lemarié, D.G. Schlom, L. Méchin, La0.7Sr0.3MnO3 suspended microbridges for uncooled bolometers made using reactive ion etching of the silicon substrates, Microelectron. Eng. 111 (2013) 101–104, https://doi.org/10.1016/j.mee.2013.02.024.
[21] D. Fobes, E. Vehstedt, J. Peng, G.C. Wang, T.J. Liu, Z.Q. Mao, Metal-insulator transition in doped Ca2RuO4: potential application in bolometric detection, J. Appl. Phys. 111 (2012) 1–6, https://doi.org/10.1063/1.4704387.
[22] D.G. McDonald, R.J. Phelan, Passivation, transition width, and noise for YBCO bolometers on silicon, IEEE Trans. Appl. Supercond. 9 (1999) 4471–4474, https://doi.org/10.1109/77.784018.
[23] R. Lu, J.J. Shi, F.J. Baca, J.Z. Wu, High performance multiwall carbon nanotube bolometers, J. Appl. Phys. 108 (2010), 084305, https://doi.org/10.1063/1.3492633.
[24] U. Sassi, R. Parret, S. Nanot, M. Bruna, S. Borini, D. De Fazio, Z. Zhao, E. Lidorikis, F.H.L. Koppens, A.C. Ferrari, A. Colli, Graphene-based mid-infrared room-temperature pyroelectric bolometers with ultrahigh temperature coefficient of resistance, Nat. Commun. 8 (2017) 1–10, https://doi.org/10.1038/ncomms14311.
[25] R. Jiménez, M. Moreno, A. Torres, P. Rosales, V. Gomez, N. Carlos, P. Roca i Cabarrocas, Effect of pressure and flow rates on polymorphous silicon-germanium (pm-Si x Ge 1−x:H) thin films for infrared detection applications, Phys. Status Solidi 215 (2018) 1700735, https://doi.org/10.1002/pssa.201700735.
[26] H. Kawazoe, M. Yasukawa, H. Hyodo, M. Kurita, H. Yanagi, H. Hosono, P-type electrical conduction in transparent thin films of CuAlO2, Nature 389 (1997) 939–942, https://doi.org/10.1038/40087.
[27] K.P. Ong, K. Bai, P. Blaha, P. Wu, Electronic structure and optical properties of AFeO2 (A = Ag, Cu) within GGA calculations, Chem. Mater. 19 (2007) 634–640, https://doi.org/10.1021/cm062481c.
[28] D.O. Scanlon, A. Walsh, G.W. Watson, Understanding the p-type conduction properties of the transparent conducting oxide CuBO2: a density functional theoryanalysis, Chem. Mater. 21 (2009) 4568–4576, https://doi.org/10.1021/cm9015113.
[29] H.-Y. Chen, J.-H. Wu, Transparent conductive CuFeO2 thin films prepared by sol–gel processing, Appl. Surf. Sci. 258 (2012) 4844–4847, https://doi.org/10.1016/j.apsusc.2012.01.022.
[30] S. Nandy, A. Banerjee, E. Fortunato, R. Martins, A review on Cu2O and Cu-based p-type semiconducting transparent oxide materials: promising candidates for new generation oxide based electronics, Rev. Adv. Sci. Eng. 2 (2013) 273–304, https://doi.org/10.1166/rase.2013.1045.
[31] Y. Wang, Y. Gu, T. Wang, W. Shi, Structural, optical and electrical properties of Mg-doped CuCrO2 thin films by sol-gel processing, J. Alloys Compd. 509 (2011) 5897–5902, https://doi.org/10.1016/j.jallcom.2011.02.175.
[32] E. Mugnier, A. Barnabé, P. Tailhades, Synthesis and characterization of CuFeO2 + δ delafossite powders, Solid State Ionics 177 (2006) 607–612, https://doi.org/10.1016/j.ssi.2005.11.026.
[33] E. Elgazzar, A. Tataroğlu, A.A. Al-Ghamdi, Y. Al-Turki, W.A. Farooq, F. El-Tantawy, F. Yakuphanoglu, Thermal sensors based on delafossite film/p-silicon diode for low-temperature measurements, Appl. Phys. Mater. Sci. Process 122 (2016), https://doi.org/10.1007/s00339-016-0148-y.
[34] Y. Lu, T. Nozue, N. Feng, K. Sagara, H. Yoshida, Y. Jin, Fabrication of thermoelectric CuAlO2 and performance enhancement by high density, J. Alloys Compd. 650 (2015) 558–563, https://doi.org/10.1016/j.jallcom.2015.08.013.
[35] T.C. Than, B.T. Bui, B. Wegmuller, M.H. Nguyen, L.H. Hoang Ngoc, V.D. Bui, Q.H. Nguyen, C.H. Hoang, T. Nguyen-Tran, Optical study of cuprous oxide and ferric oxide based materials for applications in low cost solar cells, J. Electron. Mater. 45 (2016) 2407–2414, https://doi.org/10.1007/s11664-016-4353-4.
[36] A. Barnabé, E. Mugnier, L. Presmanes, P. Tailhades, Preparation of delafossite CuFeO2 thin films by rf-sputtering on conventional glass substrate, Mater. Lett. 60 (2006) 3468–3470, https://doi.org/10.1016/j.matlet.2006.03.033.
[37] R.A. Wood, Chapter 3 Monolithic silicon microbolometer arrays, in: Semicond. Semimetals, 1997, pp. 43–121d, https://doi.org/10.1016/S0080-8784(08)62689-7.
[38] E.A. Davis, N.F. Mott, Conduction in non-crystalline systems V. Conductivity, optical absorption and photoconductivity in amorphous semiconductors, Philos. Mag. A 22 (1970) 903–922, https://doi.org/10.1080/14786437008221061.
[39] M. Shasti, A. Mortezaali, Numerical study of Cu2O, SrCu2O2, and CuAlO2 as hole-transport materials for application in perovskite solar cells, Phys. Status Solidi Appl. Mater. Sci. 216 (2019) 1–10, https://doi.org/10.1002/pssa.201900337.
[40] M.-S. Miao, S. Yarbro, P.T. Barton, R. Seshadri, Electron affinities and ionization energies of Cu and Ag delafossite compounds: a hybrid functional study, Phys. Rev. B 89 (2014), 045306, https://doi.org/10.1103/PhysRevB.89.045306.
[41] H. Jiang, X. Wang, X. Zang, W. Wu, S. Sun, C. Xiong, W. Yin, C. Gui, X. Zhu, Electronic properties of bivalent cations (Be, Mg and Ca) substitution for Al in delafossite CuAlO2 semiconductor by first-principles calculations, J. Alloys Compd. 553 (2013) 245–252, https://doi.org/10.1016/j.jallcom.2012.11.101.
[42] J.P. Hu, D.J. Payne, R.G. Egdell, P.-A. Glans, T. Learmonth, K.E. Smith, J. Guo, N.M. Harrison, On-site interband excitations in resonant inelastic x-ray scattering from Cu2O, Phys. Rev. B 77 (2008) 155115, https://doi.org/10.1103/PhysRevB.77.155115.
[43] Z.Q. Yao, B. He, L. Zhang, C.Q. Zhuang, T.W. Ng, S.L. Liu, M. Vogel, A. Kumar, W.J. Zhang, C.S. Lee, S.T. Lee, X. Jiang, Energy band engineering and controlled p-type conductivity of CuAlO2 thin films by nonisovalent Cu-O alloying, Appl. Phys. Lett. 100 (2012), 062102, https://doi.org/10.1063/1.3683499.
[44] M. Nolan, S.D. Elliott, The p-type conduction mechanism in Cu2O: a first principles study, Phys. Chem. Chem. Phys. 8 (2006) 5350–5358, https://doi.org/10.1039/b611969g.
[45] M. Currie, M.A. Mastro, V.D. Wheeler, Characterizing the tunable refractive index of vanadium dioxide, Opt. Mater. Express 7 (2017) 1697, https://doi.org/10.1364/OME.7.001697.
[46] B. Van Bilzen, P. Homm, L. Dillemans, C.Y. Su, M. Menghini, M. Sousa, C. Marchiori, L. Zhang, J.W. Seo, J.P. Locquet, Production of VO2 thin films through post-deposition annealing of V2O3 and VOx films, Thin Solid Films 591 (2015) 143–148, https://doi.org/10.1016/j.tsf.2015.08.036.
[47] D.T. Pierce, W.E. Spicer, Electronic structure of amorphous Si from photoemission and optical studies, Phys. Rev. B 5 (1972) 3017–3029, https://doi.org/10.1103/PhysRevB.5.3017.
[48] R. Jimenez, M. Moreno, A. Torres, A. Morales, A. Ponce, D. Ferrusca, J. Rangel-Magdaleno, J. Castro-Ramos, J. Hernandez-Perez, E. Cano, Fabrication of microbolometer arrays based on polymorphous silicon–germanium, Sensors 20 (2020) 2716, https://doi.org/10.3390/s20092716.
[49] N.H. Do, N.H.M. Dang, T.T. Vu, Q.H. Nguyen, N.C. Do, T. Nguyen-Tran, Selected-area growth of nickel micropillars on aluminum thin films by electroless plating for applications in microbolometers, J. Sci. Adv. Mater. Devices. 2 (2017) 192–198, https://doi.org/10.1016/j.jsamd.2017.05.004.